LASER INTERFEROMETER GRAVITATIONAL WAVE OBSERVATORY
--LIGO—
California Institute of Technology
Massachusetts Institute of Technology

Document Number: **LIGO- T020144-00-R** Date: 09/28/02

Authors: Marcus Benna, Alan Weinstein

Wavefront Sensing in Dual-Recycled Interferometers

This is an internal working note
of the LIGO Laboratory.

California Institute of Technology
LIGO Laboratory, MS 18-34
1200 E. California Blvd.
Pasadena, CA 91125
Phone (626) 395-3064
Fax (626) 304-9834

Massachusetts Institute of Technology
LIGO Laboratory, NW17-161
175 Albany St.
Cambridge, MA 01239
Phone (617) 253-4824
Fax (617) 253-7014

LIGO Hanford Observatory
P.O. Box 159
Richland, WA 99352
Phone (509) 372-8106
Fax (509) 372-8137

LIGO Livingston Observatory
P.O. Box 940
Livingston, LA 70754
Phone (225) 686-3100
Fax (225) 686-7189

Wavefront Sensing in Dual-Recycled Interferometers

An Analytical Model of Angular Alignment Signals in an Advanced Laser Interferometer Gravitational-Wave Detector

Marcus K. Benna,
King's College, University of Cambridge

Mentor: Prof. Alan J. Weinstein,
California Institute of Technology

LIGO summer undergraduate research program 2002

Abstract: The Laser Interferometer Gravitational Wave Observatory (LIGO) aims to experimentally verify for the first time ever the existence of gravitational waves predicted by Einstein's General Theory of Relativity. In order to achieve the necessary sensitivity and locking stability, it is of paramount importance not only to keep the lengths of the optical cavities constant to better than 10^{-13}m rms, but also to accurately control the angular degrees of freedom of the optics and suppress any fluctuations greater than 10^{-8} rad rms. In order to sense small angular misalignments of the optics and correct for it via a feedback control system, a wavefront sensing scheme has to be implemented. In this paper we present a derivation of a simple analytical model of alignment sensing in dual recycled interferometers, which allows us to calculate the effects of tilted mirrors and hence construct the applicable wavefront sensing matrix, relating the individual angular degrees of freedom to the signals at various output ports and at different demodulation frequencies. We show that for the Advanced LIGO optical configuration two pairs of resonant sidebands are sufficient to discriminate between misalignments in different mirrors, and propose changes in the system parameters to reconcile the requirements of length and alignment sensing.

Keywords: LIGO, gravitational waves, laser interferometry, wavefront sensing, dynamical alignment of mirrors, alignment sensing and control, ASC.

1. Introduction

Given the quadrupolar nature of gravitational radiation that ever so slightly stretches space along one transverse direction and compresses it perpendicular to that, an interferometer seems to be the natural choice of apparatus to go about detecting these feeble undulations of space-time, by measuring the phase shift between light traveling down orthogonal arms. It's a fascinating, but unsurprising fact and a demonstration of the persistence of clever ideas in physics, that essentially the same experimental setup that Michelson used a century ago to reject the aether-hypothesis and thereby corroborate the notion of the constancy of the speed of light independent of the choice of inertial frame, one of the pillars of special relativity, should now be employed to verify one of the most far-reaching predictions of Einstein's general theory of relativity, namely the existence of gravitational waves.

While at the 40m laboratory at Caltech a prototype for future Advanced Laser Interferometer Gravitational-Wave Observatories (Advanced LIGO, see [1] and [2]) is already being built, the first generation of full-scale LIGO detectors is just about to commence their initial science run and we are closer than ever before not only to confirming the existence of gravitational radiation, but also to opening up a completely new window to the universe, by making a yet entirely unexplored, new spectrum available to astronomy (see [3]-[5] for a readable undergraduate-level introductions to the subject of gravitational waves and their detection).

However, successful detection requires equipment capable of measuring strains as tiny as 10^{-21}. In order to achieve the necessary sensitivity it is essential to reduce noise from various sources (amongst others seismic, thermoelastic, radiation pressure and shot noise) to an absolute minimum and to control the mechanical degrees of freedom of the optical cavities to great accuracy. In order to lock the interferometer (prevent the laser light from falling out of resonance by continuous feedback to laser frequency and mirror position) the lengths of the various cavities have to be dynamically adjusted to within 10^{-13}m. Such strict requirements rule out the possibility of rigid attachment of the mirrors to an optical table, and instead we have to follow a completely different approach, namely to suspend the optics from wire loops (see Figure 1), which act like a pendulum and hence provide seismic isolation at frequencies higher than about 1Hz, the mechanical resonance frequency, while keeping the mass free to move horizontally in response to gravitational waves in the LIGO band between about 40Hz and 2000Hz. Note that Advanced LIGO will have multiple pendulum stages including blade springs to further enhance both horizontal and vertical isolation.

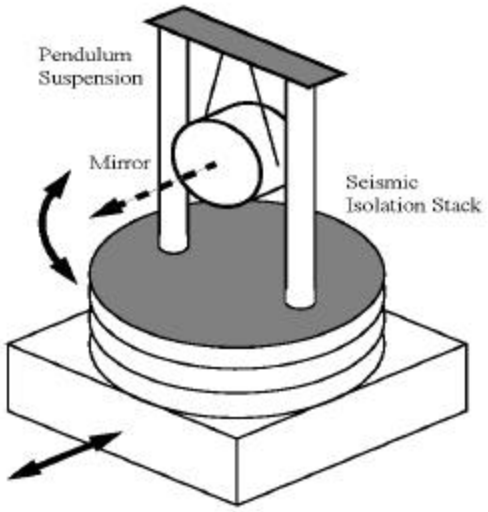

Figure 1: Suspended mirror.

Another aspect of ensuring stable locking and low noise levels, which at such extremely high levels of precision becomes almost equally important due to the pendular nature of the suspensions, is to control the rotations of the mirrors. Fritschel et al. [6] have calculated an upper limit to angular fluctuations of 10^{-8}rad rms for a LIGO-like kilometer scale interferometer and furthermore discuss the maximum admissible spectra of pointing and displacement fluctuations of the beam delivered to the core interferometer, which sets the requirements for the input optics. The latter does not concern us here and we start from the assumption that the incoming laser beam is sufficiently stable with respect to the beam splitter (BS), which we will use as our reference for all angular misalignments. Violation of the angular alignment requirements would lead to loss of effective beam power (due to coupling into higher order modes as we shall see below), introduction of excess technical noise and corruption of the interference pattern at the dark port by leaking out of higher order modes, which would increase the photocurrent and could even introduce fake gravitational wave signals. Hence we need to implement a feedback control loop, which continuously corrects for any angular misalignments.

In initial LIGO the actuation is performed by five optical sensor electromagnetic actuator units (OSEMs), each consisting of an arrangement of a coil, a light emitting diode (LED) and a photodiode attached to the suspension frame of each mirror, plus a small magnet glued to the mirror itself. This system can detect its position, pitch (rotation about the horizontal axis) and yaw (rotation about the vertical axis), by measuring the degree to which the magnet eclipses the LED, and move the mirror by varying the current in the coils.

Hence we have a way of adjusting the angular degrees of freedom of each mirror, which will constitute the final stage of our control system. However, the information obtained from the optical sensors is much too crude to be of any use to us, in particular since the measuring system is part of the suspension frame, which even though it sits on seismic isolation stacks is not perfectly at rest with respect to the mirror. This motivates the implementation of a more sophisticated alignment detection scheme.

We can achieve this goal by using a technique termed wavefront sensing, which employs the light itself as the measuring device analogously to the detection of the differential length change of the arms by observing the phase shift at the dark port. In order to realize such a scheme we have to place quadrant detector photodiodes at various output ports to pick off light from different stages of the interferometer and use the fact that beats between the carrier light and the sidebands (required for length sensing) can be employed to infer angular misalignments. We will determine the optimal positions and demodulation phases of those quadrant detector photodiodes, as well as a scheme for converting their output into a set of useful error signals, that allow us to discriminate between the misalignments of the different mirrors (by diagonalizing the so-called wavefront sensing matrix connecting mirror rotation angles and sensor responses as far as possible). Thus we can accurately correct for misalignments by acting on the tilted optic only.

For the initial LIGO detectors this calculation was performed by the "Modal Model" software package, which was developed by D. Sigg and N. Mavalvala using a matrix approach (see [7] and [8]). While it was hoped that the results for the more complex Advanced LIGO configuration could be obtained in the same way, this turned out to be highly problematic, and hence we devised our own model of wavefront sensing in Advanced LIGO interferometers, based entirely on analytical expressions for every step leading to the final error signals that are fed into the control system.

In Section 2 we give an outline of the layout of the second generation of LIGO detectors as currently envisioned and Section 3 provides a brief review of Gaussian beams in resonant cavities, the Pound-Drever-Hall reflection locking technique and its extension to alignment sensing. We present our derivation of a simple analytical model of alignment signals in dual-recycled interferometers in Section 4 and finally discuss our results in Sections 5 and 6.

2. The Optical Configuration and Control Scheme of Advanced LIGO

The optical configuration of Advanced LIGO (see [2]) is most easily understood by starting from a simple Michelson arrangement consisting of a source of coherent light, in our case a Nd^{3+}:YAG laser emitting infrared radiation at a wavelength of 1.064 μm, a BS dividing the incident light power equally between two perpendicular arms and two mirrors terminating the arms which coincide with the end test masses (ETMs) in LIGO. In principle these components alone are sufficient to carry out interferometry and detect small length changes to a precision only bounded by the standard quantum limit, but practical considerations lead us to add more optical elements.

From astrophysical considerations of understood sources of strong gravitational radiation we know that we cannot expect any detectable signals at frequencies greater than a few kHz because a mechanism that could coherently move stellar-sized masses at such high frequencies has yet to be conceived. Given a lower frequencies limit for earthbound interferometers of the order of 10Hz, set by unavoidable seismic noise, the LIGO science collaboration chose the peak sensitivity to lie in the region of about 100Hz, which still confines the range of observable events to the most violent and energetic processes imaginable, such as the last few seconds of spiraling in and the final coalescence of two compact objects or non-spherically symmetric supernovae.

To maximize the susceptibility of our apparatus to such events we need to increase the storage time of light in the arms in order to

multiply the phase shift, which is the quantity we actually measure, for any given strain of the arm cavities. The obvious way to achieve this is to increase the length of the arms, but for terrestrial interferometers practical considerations set a limit to the dimensions of our apparatus, which forces us to follow a different route, namely to fold the light path. We can achieve this by adding two input test masses (ITMs) that turn our arms into Fabry-Perot cavities, such that the laser beam effectively makes several hundred round trips before leaking out towards the BS[1]. The optimal storage time is of the order of a half a period of the gravitational wave frequency, such as to accumulate the maximal phase shift.

Now the lengths of the Fabry-Perot cavities will be adjusted microscopically such that the laser light is on resonance, and the optical path lengths between the BS and the ITMs such that the light interferes destructively at the anti-symmetric port (hence also called dark port). This implies that in the absence of a perturbation, such as that caused by a passing gravitational wave, all the carrier light would pour out the symmetric (bright) port and be lost. However, there is an optimal laser power set by the interplay of shot noise, dominant at high frequencies and decreasing with laser power as $1/\sqrt{P_{laser}}$, and radiation pressure noise, important at low frequencies and growing with laser power as $\sqrt{P_{laser}}$. These two fundamental noise sources[2] define the so-called standard quantum limit, an uncertainty relation limiting the precision to which we can continuously monitor the differential length change for the initial LIGO design. The optimal laser power would be the one at which we can just reach the quantum limit at the design frequency. Those considerations would suggest an optimal laser power in the arm cavities of the order 1MW, which is an order of magnitude greater than what initial LIGO achieves, while Advanced LIGO will operate at the optimized power level. It would be a waste of valuable laser power to just let the light heading towards the bright port of the BS escape and hence we add a so-called power-recycling mirror (PRM) in order to feed this light back into the interferometer coherently, thus substantially increasing the power levels in the system. The power-recycling cavity (PRC) formed by the PRM and the ITMs must also be kept on resonance (see Figure 2).

The most obvious change in upgrading to the Advanced LIGO design will be the addition of an additional optic, termed signal-recycling mirror (SRM), at the dark port of the signal. Despite the similar arrangement (hence the adjective dual-recycled) it serves a completely different purpose to the PRM. While in the unperturbed state there will be no carrier light arriving at the dark port, the audio-frequency sidebands imposed by gravitational waves will pour out of the dark port, as they constitute a differential signal. The SRM can modify the response of the interferometer to gravitational waves and in particular reshape the limiting noise curve. Several schemes are conceivable, differing from each other by the tuning of the signal-recycling cavity (SRC). Extreme signal recycling has the SRC resonant for the carrier such that the storage time for the gravitational-wave audio-sidebands is increased, while extreme resonant sideband extraction has the SRC exactly anti-resonant, so that the audio-sidebands are extracted from the arm cavities. In practice the most favorable arrangements have a tuning $0<d\nu<\pi/2$ in between these two depending on the frequency we wish to optimize our sensitivity for, and it has been shown that over a limited frequency range dual-recycled interferometers can even beat the standard quantum limit (see [9]).

This leaves us with five relevant length degrees of freedom (see Figure 2 for definitions), the common and differential arm cavity lengths, $(L_A+L_B)/2$ and $(L_A-L_B)/2$ respectively, the differential Michelson length L_2-L_3, as well as the lengths of the PRC and the SRC, $L_{PRC}=L_1+(L_2+L_3)/2$ and $L_{SRC}=(L_2+L_3)/2+L_4$ respectively[3]. The macroscopic value of L_2-L_3 is also known as Schnupp asymmetry. In order to dynamically control these lengths, two radio

[1] This arrangement is preferable to a Delay Line Interferometer, in which the different round trip beams are spatially separated, because the maximum size of the mirrors limits the possible number of round trips.

[2] In a proper quantum-mechanical description these are really two facets of the same fundamental noise, the radiation pressure noise being the back-action of the quantum fluctuations in the shot noise and thus describing the way in which the measurement disturbs the system to be measured.

[3] There is no need to control the potential sixths degree of freedom, the common Michelson length $(L_2+L_3)/2$, or equivalently L_1, because the operation of the interferometer is invariant under a change in this quantity.

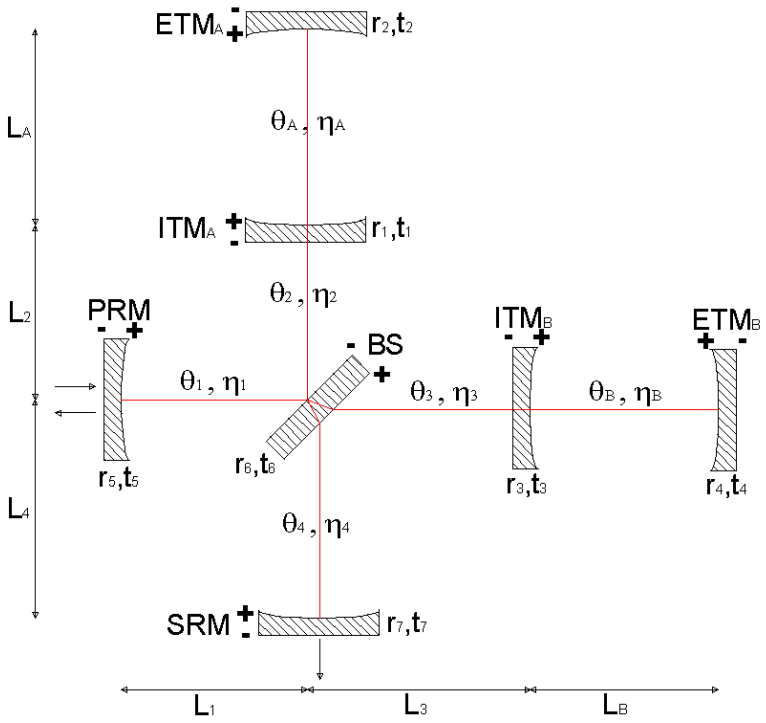

Figure 2: Optical configuration and parameters of a dual-recycled interferometer.

frequency (RF) sidebands are imposed on the laser light through phase modulation by Pockels cells, before it enters the interferometer, which can then be employed to keep the cavities on resonance by Pound-Drever-Hall locking as outlined below.

One of the sideband (difference) frequencies, $\Delta\omega_2$, is chosen to be as high as possible, limited to about 200MHz by current technology of RF photodetectors and demodulation electronics, the other frequency, $\Delta\omega_1$, is set to be as low as the dimensions of the PRC allow, as it has to be resonant there and the PRC in turn has to fit into a vacuum envelope. Both sidebands must be transmitted by the mode cleaner that the light is passed through before it enters the core optics and hence their frequencies must be multiples of its free spectral range.

The current design (see [1]) is optimized for high sideband power in the recycling cavities only, and the idea behind it is to have the upper sideband of the higher modulation frequency resonant in both the PRC and the SRC, while the lower frequency pair of sidebands is resonant in the PRC only (see Figure 3). According to this scheme (for a crude optimization of the power levels only, without regard of the requirements for alignment sensing) the following choice of lengths and frequencies has been suggested:

$$L_{PRC} = (l + 1/2)\frac{2pc}{2\Delta w_1}, \tag{1a}$$

$$\Delta w_2 = m\Delta w_1, \tag{1b}$$

$$L_2 - L_3 = \frac{2pc}{4\Delta w_2}, \tag{1c}$$

$$L_{SRC} = (n - dn/2)\frac{2pc}{2\Delta w_2} - L_{PRC}, \tag{1d}$$

where *l, m and n* are integers. These equations impose the conditions that the lower frequency sideband be resonant in the PRC, the dark port of the interferometer be bright for the frequencies $\omega \pm \Delta\omega_2$ and that the upper sideband of frequency $\Delta\omega_2$ be resonant in the SRC.

We wish to use the very same sidebands to also control the angular degrees of freedom of the interferometer. Choosing the BS as a reference we can describe those in terms of differential and common arm cavity, and recycling cavity modes, as we have done for the lengths. This leads to twelve distinct angular degrees of freedom, six for pitch, and six for yaw (the latter are shown in **Figure 4**).

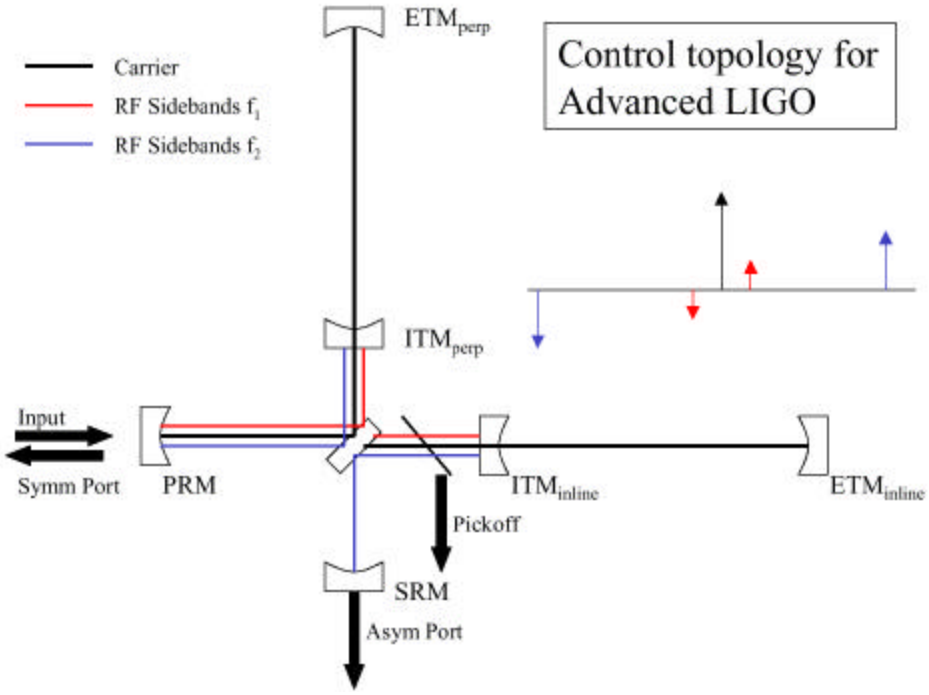

Figure 3: Advanced LIGO control scheme.

The depicted degrees of freedom are not actually the normal modes of the system (which would be the axes of a six-dimensional variance ellipsoid describing the reduction of sensitivity as a function of relative motion in the six degrees of freedom) but we will refer to them as modes for convenience.

In this picture a rotation of the BS is equivalent to appropriate misalignments of the other six mirrors. However, as is easy to visualize, this would cause the beam spots on the mirrors to move off centre, most severely so on the ETMs due to the great length of the arms. Fritschel et al. [6] have estimated that this effect would be detrimental to the sensitivity if the beam centroid were displaced by more than 1mm from the center of rotation of the ETM. To prevent this from happening, a separate monitoring system must be implemented to ensure that gradual drift during the operation of the alignment control system doesn't displace the beam too much from the center of the mirror.

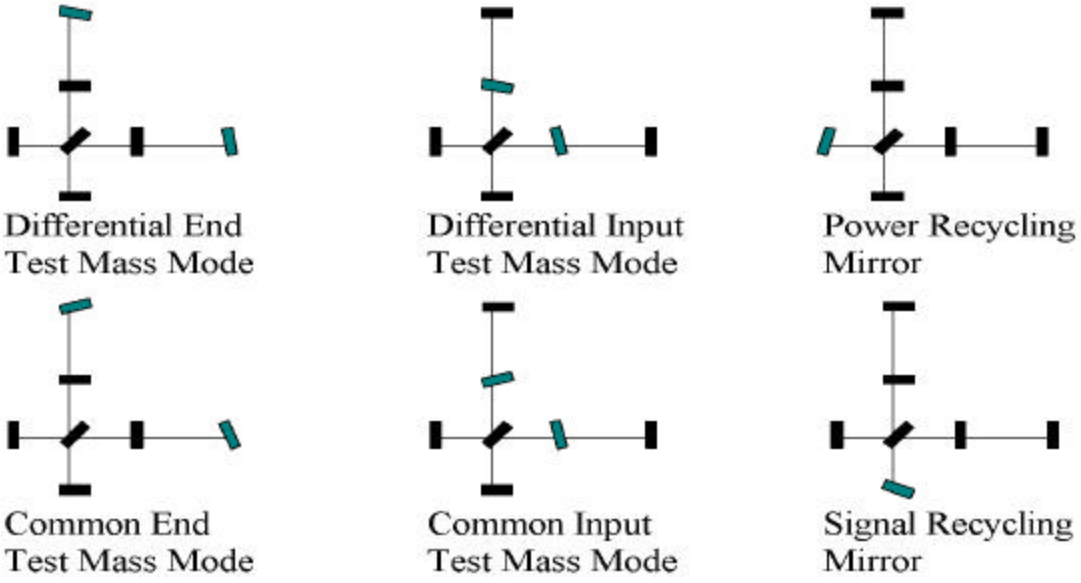

Figure 4: Angular degrees of freedom of a dual-recycled interferometer in one dimension.

3. Gaussian Beam Optics, Resonant Cavities, Pound-Drever-Hall Locking and Wavefront Sensing

3.1. Fundamental Gaussian Beam

In contrast to a plane wave, a laser beam is finite in transverse extent and the simplest solution of the wave equation (for one particular polarization) that fulfills this requirement is a Gaussian beam (see[10]-[12]) described by:

$$\begin{aligned} &E(x,y,z) = \\ &= E_0 \frac{w_0}{w(z)} \exp\left\{-i[kz - h(z)] - i\frac{k(x^2+y^2)}{2q(z)}\right\} = \\ &= E_0 \frac{w_0}{w(z)} \exp\{-i[kz - h(z)]\} \\ &\exp\left\{-(x^2+y^2)\left[\frac{1}{w^2(z)} + \frac{ik}{2R(z)}\right]\right\}, \end{aligned} \tag{2}$$

where z is the distance from the so-called waist, the point of minimum beam diameter, and w_0 is the characteristic width or spot size at the waist (the radius at which the amplitude has fallen to 1/e of its peak value). The width elsewhere along the axis of the beam is given by

$$w(z) = w_0 \sqrt{1 + \frac{z^2}{z_0^2}}, \tag{3}$$

while

$$R(z) = z\left(1 + \frac{z_0^2}{z^2}\right) \tag{4}$$

is the radius of curvature of the wavefronts and

$$h(z) = \tan^{-1}\left(\frac{z}{z_0}\right) \tag{5}$$

is the Guoy phase shift. Information about the radius of curvature of the wavefronts and the width of the beam is often combined in the complex beam parameter q:

$$\frac{1}{q(z)} = \frac{1}{R(z)} - i\frac{2}{kw^2(z)}. \tag{6}$$

The characteristic length scale of the beam, the so-called Rayleigh length, is defined as:

$$z_0 \equiv \frac{pw_0^2}{l}. \tag{7}$$

We see that the Gaussian envelope restricting the transverse extent of the beam entails two more crucial differences from a plane wave. Firstly, the wavefronts are spherical rather than flat (except at the waist, where their radius of curvature becomes infinite), and secondly there is an additional phase shift, termed Guoy phase shift, that is accrued largely within a distance of one Rayleigh length either side of the waist (see Figure 5).

The surfaces of constant amplitude are the hyperboloids given by (3), which implies that far from the waist the beam asymptotically approaches a constant divergence angle of $\lambda/\pi w_0$, the far field diffraction angle.

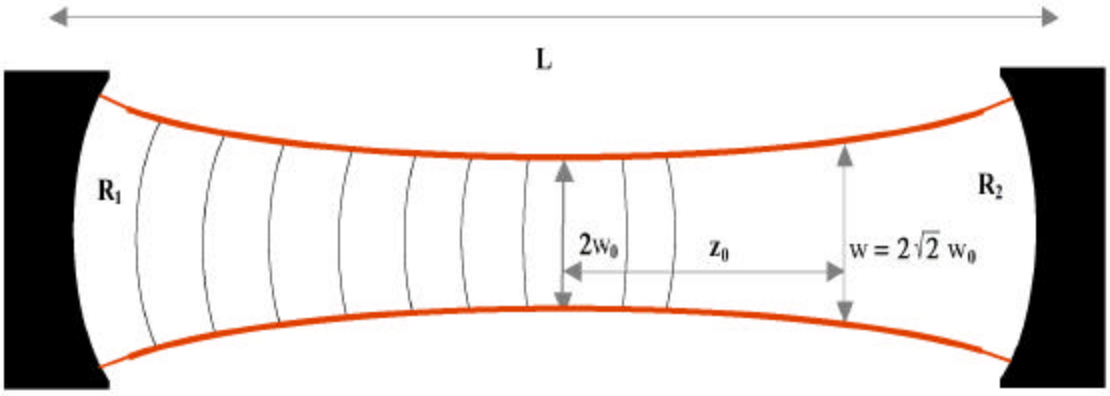

Figure 5: Gaussian beam in an optical cavity.

3.2. Optical Cavities and Hermite-Gaussian Modes

If we were to obstruct the beam with two mirrors shaped so as to match the curvature of the wavefronts at their respective positions, the traveling wave would be exactly reflected back onto itself, and we would obtain a steady state field configuration (an eigenmode) also described by (2) except that the time dependence (which we have dropped here) would be that of a standing wave. In a real Fabry-Perot cavity, what happens is the opposite: The distance and radii of curvature of the mirrors uniquely determine the steady state Gaussian beam eigenmode, by fixing the location of the waist and the minimum spot size.

Of course a two-dimensional Gaussian is not the only possible transverse profile and in fact any beam shape with an arbitrary functional dependence on x and y can be expressed as a linear combination of Hermite-Gaussian modes, which form a complete orthogonal set of functions and are most convenient in Cartesian coordinates:

$$E_{lm}(x,y,z) = E_0 \frac{w_0}{w(z)} H_l\left(\sqrt{2}\frac{x}{w(z)}\right) H_m\left(\sqrt{2}\frac{y}{w(z)}\right) \exp\left\{-ikz + i(l+m+1)\eta(z) - i\frac{k(x^2+y^2)}{2q(z)}\right\}, \quad (8)$$

where H_l are the Hermite polynomials, well known from the quantum mechanical solution of the simple harmonic oscillator. In particular, $H_0(x)=1$ and $H_1(x)=x$, are the only ones we are interested in here, so that if we include the complete transverse dependence in one dimension in a normalized function $U(x)$ we obtain:

$$U_0(x) = \left(\frac{2}{\pi w_0^2}\right)^{1/4} \exp\left[-\left(\frac{x}{w_0}\right)^2\right], \quad (9)$$

$$U_1(x) = \left(\frac{2}{\pi w_0^2}\right)^{1/4} \frac{2x}{w_0} \exp\left[-\left(\frac{x}{w_0}\right)^2\right]. \quad (10)$$

We denote higher order modes with a transverse dependence $U_l(x)U_m(y)$ by TEM_{lm}, where TEM is short for transverse electromagnetic mode. Note that higher order modes differ not only in their intensity cross section, but also have a higher Guoy phase shift due to the $(l+m+1)\eta(z)$ term in (8), which implies a different resonant frequency in an optical cavity. The resonance condition for TEM_{lm} in a cavity of length L, consisting of two mirrors placed at distances z_1 and z_2 from the waist, is then given by:

$$kL - (l+m+1)\left(\tan^{-1}\frac{z_2}{z_0} - \tan^{-1}\frac{z_1}{z_0}\right) = p\pi \ , \quad (11)$$

where p is an integer.

3.3. Pound-Drever-Hall Locking

Equation (11) implies that we have to control the length of the optical cavity to a small fraction of a wavelength of the laser light and this can be achieved using the Pound-Drever-Hall reflection locking technique (see [13]), which we will very briefly explain here, because alignment sensing can be viewed as an extension of the same idea. It employs two well known experimental concepts: Firstly, we use the principle of a lock-in amplifier to extract a weak signal from a large, noisy background, and secondly, we choose this error signal such that it is zero-crossing at the optimal operating point and linear in its neighborhood. Our length control system is therefore an active null device (see Figure 6).

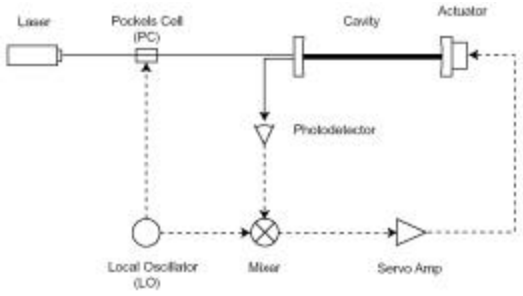

Figure 6: Principles of Pound-Drever-Hall locking.

The laser light is RF phase-modulated by a Pockels cell before entering the cavity, which can be described as an addition of sidebands (see Section 4.5), whose frequencies are chosen such that they are not resonant in the cavity and instead are promptly reflected off the front mirror. The carrier frequency on the other hand is ideally resonant in the cavity and thus probes the back mirror. We observe the intensity variation on a photodiode at the reflected port,

which includes an interference term between carrier and sidebands varying at the chosen (radio) frequency. Demodulating this intensity time series with the help of the same local oscillator (to guarantee coherence with the initial modulation, as in a lock-in) we obtain an error signal carrying information about the length of the cavity. Choosing the demodulation phase correctly we can arrange that it crosses zero when the cavity is on resonance. By observing the beats between carrier and sidebands we effectively measure the phase of the carrier light leaving the cavity, rather than its intensity, which has the advantage of varying linearly, rather than quadratically with the deviation from resonance, thus being much easier to handle and telling us immediately the sign of the required length change. The error signal can then be fed into a servo driving an actuator such as the OSEMs described above to make the necessary adjustments to the position of one of the mirrors.

3.4. Alignment Sensing

Alignment sensing rests on a very similar principle, except that the interference we observe in this case is not between the TEM_{00} of carrier and sidebands, but between the TEM_{00} and the TEM_{10} of those two frequencies (see Figure 7).

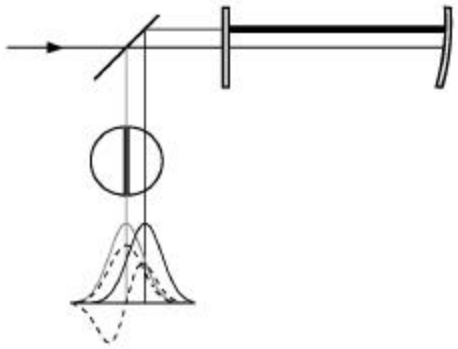

Figure 7: Principles of wavefront sensing. The sidebands are reflected back along the nominal beam axis (grey), but the back mirror is misaligned and hence the carrier light hits the photodiode off center (black, with modal decomposition into TEM_{00} and TEM_{10}, dashed)

Again we send a sideband-endowed laser beam into an optical cavity, choosing the RF-modulation frequency such that the sidebands aren't resonant. Assuming that the front mirror was perfectly aligned, the sidebands would thus be directly reflected back along the nominal axis of the beam. The carrier light however, enters the cavity and encounters the misaligned back mirror, which causes the beam to be tilted with respect to the nominal axis. Therefore the carrier light hits the photodetector at the output slightly off center, and as we shall see in Section 4.3, a tilted TEM_{00} beam is equivalent to linear combination of TEM_{00} and TEM_{10} in the coordinate system aligned with the nominal axis of the beam. Thus the presence of TEM_{10} signifies a misaligned mirror, and in order to detect the interference terms involving this odd transverse profile, which would average to zero on a normal photodiode, we use a split detector and subtract the intensities integrated over the two half-planes, thereby canceling out all even terms involving only TEM_{00} and again obtaining a linear, zero-crossing error signal after demodulation. From this point on alignment sensing follows the same principle of nulled lock-in operation as the Pound-Drever-Hall technique, and the OSEMs can again be used as actuators.

The major advantages this technique offers as compared to simply monitoring the shift of peak intensity on the detector due to the misalignment is that firstly we can achieve much higher accuracy without the need for a long lever arm, and secondly we can distinguish misalignments in the back and front mirror.

Note that in this picture of modal decomposition there is a crucial difference between length sensing and alignment sensing. Whereas length sensing signals make use of a phase shift in the TEM_{00} modes of the carrier and sidebands which are already present in the unperturbed situation, alignment sensing signals rely on TEM_{10} modes which have to be created at a misaligned surface in the first place. The consequences of this are twofold: Firstly, because the angles we are concerned with (and hence the coupling coefficients quantifying the relative strength of the TEM_{10} components) are small, the alignment signals resulting from the interference terms between TEM_{00} and TEM_{10} are weak compared to length sensing signals, and secondly, because TEM_{10} components propagate in a different way due to the extra Guoy-phase shift, the resulting signals are not exactly analogous to those for length sensing.

Figure 8 illustrates a possible arrangement for alignment sensing in a dual-recycled interferometer (see [14] and [15]). Six wavefront sensors are distributed amongst the output ports

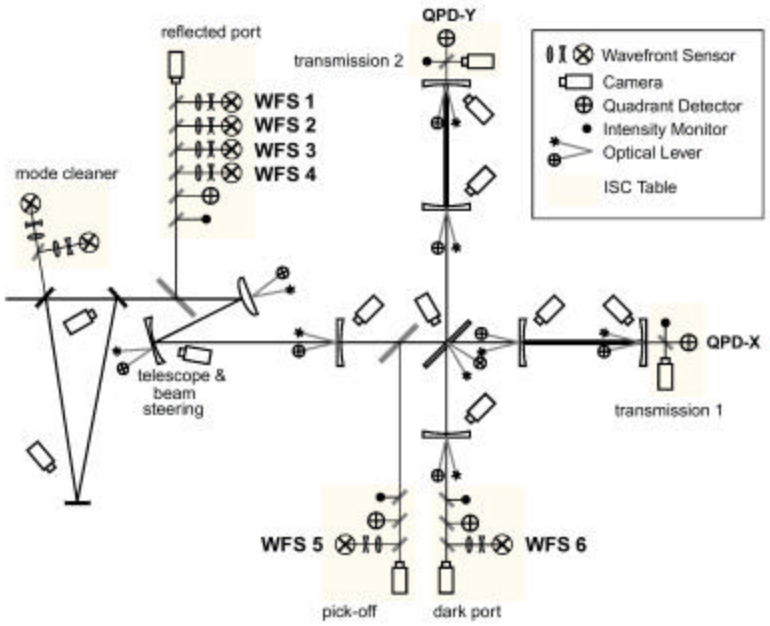

Figure 8: Possible wavefront sensing scheme for the Advanced LIGO optical configuration.

in order to discriminate between the motions in the six angular degrees of freedom. We wish to determine their optimal positions, demodulation frequencies and phases. Because we want to monitor misalignments in both pitch and yaw, we actually use quadrant photo detectors rather than simply split photodiodes, and add or subtract the contributions of the four quadrants appropriately.

Optical levers on each mirror aid initial (rough) alignment. Furthermore, each wavefront sensor is shown with an arrangement of lenses, a so-called Guoy phase telescope, between the output port and the photodiode. This allows us to introduce a Guoy phase advance of our choice before the detection stage, and as we will see below this is useful in distinguishing between different angular degrees of freedom.

4. Derivation of an analytical model of alignment sensing signals in dual-recycled interferometers

In this section we outline the derivation of the results required to obtain an analytical solution of the problem. The basic scheme is to first calculate the steady state fields of the TEM_{00} mode at all relevant points of the interferometer in the perfectly aligned state, then treat any misaligned optics as a source of TEM_{10} mode with the appropriate coupling coefficients and propagate both fields to the various output ports, where we demodulate with an appropriate choice of phases to maximize the signal.

Because the response of the interferometer to misalignments in pitch and yaw is the same to first order, we restrict all calculations to one transverse dimension. Furthermore we neglect the effects of higher order modes (i.e. consider only TEM_{00} and TEM_{10}), which in the case of a LIGO observatory is an excellent approximation for angles smaller than about one half the far field diffraction angle of the beam impinging on the mirror, as has been demonstrated by Hefetz et. al. [16]. Because the requirements on angular alignment are much stricter than this (by three orders of magnitude) our control system will always keep the system in this small angle regime.

Note also that our derivation applies only in the quasi-static approximation. The time constant for the approach of a steady state situation is of the order of the light storage time of the arm cavities, which is approximately 1ms for Advanced LIGO. On the other hand, the control system we wish to implement would operate in a frequency range of up to 10Hz at most, since the response of the mirrors is very small at frequencies large compared to its pendulum resonance, and hence a quasi-static calculation is sufficient for our purposes.

4.1. Fabry-Perot Arm Cavities

First consider a simple two-mirror Fabry-Perot cavity like the ones that form the arms of the LIGO interferometer (see Figure 9). Let the front mirror (the ITM) have amplitude transmissivity t_1 and amplitude reflectivity $\pm r_1$, while for the ETM we denote the corresponding variables by t_2 and $\pm r_2$. We use here the convention usually preferred by physicists, choosing the transmission coefficients to be real and positive, and the reflection coefficients to be real with the sign depending on the side from which the beam is incident[4]. Our sign convention is illustrated in Figure 2.

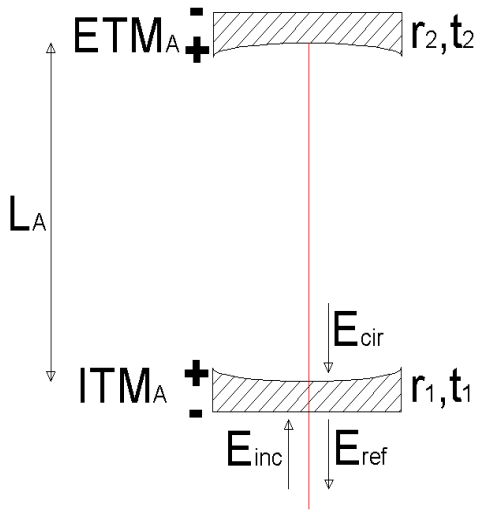

Figure 9: Definition of variables for a Fabry-Perot arm cavity.

At every mirror we have a junction condition that allows us to relate the fields on either side, such that if we denote the amplitude of the incident field by E_{inc}, of the circulating field by E_{cir} and of the reflected field by E_{ref}, we can write:

$$E_{ref} = -r_1 E_{inc} + t_1 E_{cir} . \qquad (12)$$

Note that in writing down this expression with complex field amplitudes E, we take into account the overall phase only, i.e. we do not keep track of the Guoy phase advance and the one due to the $(-kz+wt)$ term separately. This is also implicit in our propagator $\exp(-i\theta_A) = \exp(-ikL_A+i\eta_A)$, which takes into account both the Guoy phase advance η and the phase shift $-kL$ that an idealized plane wave would experience, but doesn't discriminate between the two[5]. In fact it is impossible to maintain such a distinction in this simple picture, because we are working under the assumptions that all cavities are (mode) matched to each other perfectly and the shapes of the wavefronts impinging on any mirror exactly fit its curvature, so that all modal and frequency components have the same beam parameter (i.e. the same characteristic width and radius of curvature) at any point. This allows us to characterize the fields by their complex amplitudes alone. Using the propagator and junction conditions it is trivial to derive:

$$E_{cir} = t_1 r_2 e^{-i2q_A} E_{inc} + r_1 r_2 e^{-i2q_A} E_{cir} . \qquad (13)$$

Hence we obtain the expression

$$E_{ref} = \frac{r_2(r_1^2 + t_1^2)e^{-i2q_A} - r_1}{1 - r_1 r_2 e^{-i2q_A}} E_{inc} , \qquad (14)$$

which allows us to define an effective complex reflection coefficient r_{FPA} of the arm cavity given by:

$$r_{FPA} = \frac{r_2(r_1^2 + t_1^2)e^{-i2q_A} - r_1}{1 - r_1 r_2 e^{-i2q_A}} , \qquad (15a)$$

and similarly for the second arm cavity:

$$r_{FPB} = \frac{r_4(r_3^2 + t_3^2)e^{-i2q_B} - r_3}{1 - r_3 r_4 e^{-i2q_B}} . \qquad (15b)$$

Note that on resonance the effective reflection coefficient is real, and due to the almost perfectly reflective ETM will be positive for the carrier (the cavity is said to be over-coupled, because $r_2(r_1^2+t_1^2)>r_1$ on resonance). The sidebands on the other hand are approximately anti-resonant in the arm cavities (not exactly, because otherwise their even harmonics would be resonant) so that for them the effective reflectivity is negative.

[4] This is in contrast to the engineering convention, which uses a scattering matrix with both reflection coefficients real and positive, and both transmission coefficients purely imaginary.

[5] Note carefully that here and in the following sections up to 4.5 we omit, but don't forget the time dependence of the fields.

4.2. Beam Splitter and Recycling Cavities

Having worked out the effective reflectivity of the arm cavities, we can now draw a simplified picture of the remaining interferometer (see Figure 10) which essentially consists of the two coupled recycling cavities.

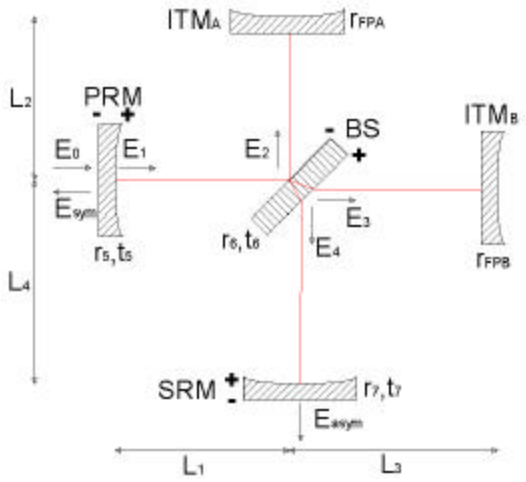

Figure 10: Definition of variables for the recycling cavities.

We denote by E_0 the amplitude of the incident light, by E_1 to E_4 the steady state fields of the TEM_{00} mode and as above by r and t the amplitude reflection and transmission coefficients of the mirrors. Using exactly the same method as in section 4.1, it is easy to derive the matrix equation:

$$\mathbf{M}_{jk}\mathbf{E}_k = \mathbf{S}_j, \tag{16}$$

where

$$\mathbf{M} = \begin{bmatrix} 1 & r_{FPA}r_5r_6e^{-i(q_1+2q_2)} & -r_{FPB}r_5t_6e^{-i(q_1+2q_3)} & 0 \\ r_6e^{-iq_1} & 1 & 0 & -t_6r_7e^{-i2q_4} \\ -t_6e^{-iq_1} & 0 & 1 & -r_6r_7e^{-i2q_4} \\ 0 & -r_{FPA}t_6e^{-i2q_2} & -r_{FPB}r_6e^{-i2q_3} & 1 \end{bmatrix} \tag{17}$$

with the subscripts of the reflection/transmission coefficients and phases accrued as shown in Figure 2. The column matrices of steady state fields **E** and source terms **S** are given by:

$$\mathbf{E} = [E_1, E_2, E_3, E_4]^T \tag{18}$$

and

$$\mathbf{S} = [t_5E_0, 0, 0, 0]^T. \tag{19}$$

It is a matter of simple linear algebra to solve for E_1 to E_4, and by propagating the fields to the output ports we are interested in we obtain:

$$E_{sym} = -r_{FPA}t_5r_6e^{-i(q_1+2q_2)}E_2 + \\ + r_{FPB}t_5t_6e^{-i(q_1+2q_3)}E_3 - r_5E_0 \tag{20a}$$

$$E_{asym} = t_7e^{-iq_4}E_4 \tag{20b}$$

In addition to observing the bright and dark port of the interferometer, we can also pick off so-called ghost rays reflected from the anti-reflection coatings of any substrate the beam passes through. Both the BS and the ITMs are equipped with wedge angles of 0.5°, which prevent the backscattered light from interfering with the main beam, and due to this spatial separation it is easy to steer such ghost beams onto a photodiode. In particular, we chose to look at a reflection from the substrate of the BS, which corresponds to extracting a small fraction of the field at E_3, such that

$$E_{pickoff} = t_6r_{AR}E_3, \tag{20c}$$

where r_{AR} is the amplitude reflectivity of the anti-reflection coating and we have neglected the phase shift accrued within the substrate (see Figure 11). Note that the loss of beam power due to unwanted reflections is accounted for in the scattering coefficients r and t of the mirrors.

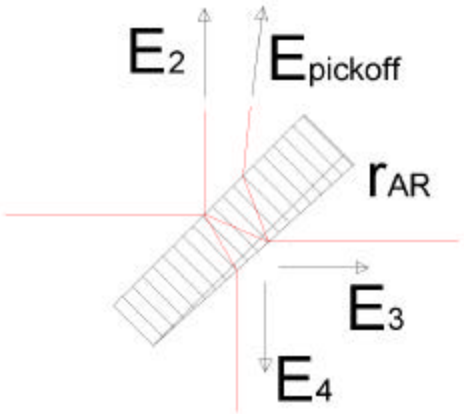

Figure 11: Pickoff from anti-reflection coating of beam splitter.

4.3. Misaligned Mirrors and Coupling into TEM_{10} Mode

We have calculated the steady state fields of the TEM_{00} mode of any given Fourier component at all relevant locations in the perfectly aligned interferometer, and so we are now in a position to ask what changes when we misalign some of the mirrors slightly. A tilt of angle α_x with respect to the nominal optical axis of a cavity results in any beams reflecting off that surface being deflected by $2\alpha_x$. If we assume for simplicity that the mirror surface was flat and that the waist of the incoming beam was placed at the mirror such that its wavefronts coincide with the surface, we can easily resolve the magnitude and phase of the off-axis electric field of the reflected beam $E(x')$ traveling along the axis z' onto the corresponding wavefronts of a TEM_{00} beam $AU_0(x)$ reflected from a perfectly aligned mirror and traveling along z (see [17]). For the magnitude of the electric field we find that to first order there is no change:

$$|E(x)| = \frac{|E(x')|}{\cos(2a_x)} \approx \approx |E(x')| \cdot (1 + 2a_x^2 + O(a_x^4)). \tag{21}$$

The phase on the other hand, which is independent of x at the waist of a Gaussian beam, where the wavefronts are planes, now depends on x because the wavefronts are tilted with respect to the coordinate axes:

$$\arg[E(x)] = \frac{2p}{l} x \sin(2a_x) \approx \frac{2px}{l} 2a_x . \tag{22}$$

The findings of equations (21) and (22) can be summarized in a complex exponential, which can be expanded as α_x is small:

$$E(x) \approx AU_0(x) \exp(i \frac{2px}{l} 2a_x) \approx \approx AU_0(x)\left[1 + i\frac{2px}{l} 2a_x + O(a_x^2)\right] \approx \approx A\left[U_0(x) + 2i\frac{a_x p w_0}{l} U_1(x)\right]. \tag{23}$$

We see that the modal decomposition allows us to express a perfectly Gaussian beam pointing in the wrong direction as a superposition of the TEM_{00} and TEM_{10} Hermite-Gaussian modes referred to the coordinate system defined by the nominal optical axis. There are two things worth noting about this equation. Firstly, for a tilt with respect to the nominal optical axis the coupling into the first order mode takes place in quad-phase (whereas for a displacement relative to the optical axis it would be in phase). Secondly, the expression $\alpha_x \pi w_0/\lambda$, the misalignment angle divided by the far field diffraction angle, is defined to be the normalized angle a'_x.

Hence for any TEM_{00} mode reflected off a misaligned surface we can treat that surface as a source of TEM_{10} mode with coupling coefficient $2ia'_x$. Note that we neglect back-coupling of TEM_{10} into TEM_{00}, which is a second order effect.

4.4. Propagation of TEM_{10} Mode

Having obtained the coupling coefficients connecting the two lowest order modes, we repeat the steps of Sections 4.1 and 4.2 for the TEM_{10} mode, this time treating not the incident beam (which we presume to have a perfectly Gaussian transverse profile), but any misaligned mirrors as sources. For any mirror surface we define a source term Δ given by the TEM_{00} field reflected off that surface multiplied by $2ia'_x$.

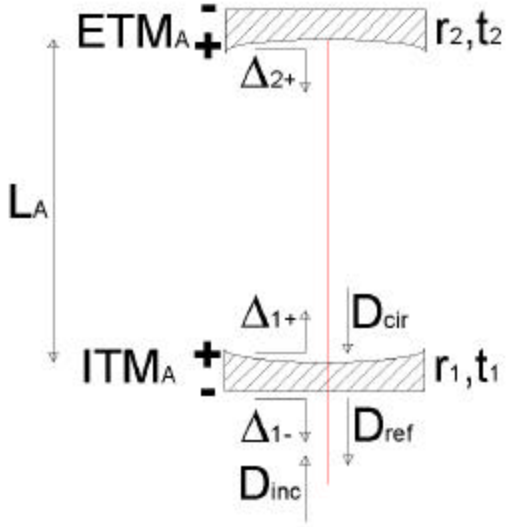

Figure 12: Variables for propagation of TEM_{10} mode in an arm cavity.

Again we can define an effective reflection coefficient for the arm cavities (see Figure 12), but this time we have to add an extra term due to

the potential sources. Denoting the electric field amplitude of the TEM$_{10}$ mode by D, we have:

$$D_{ref} = r_{FPA} D_{inc} + \Delta_A, \tag{24}$$

where r_{FPA} is defined as in (15a), and

$$\Delta_A = \frac{t_1 r_2 e^{-i2q_A}\Delta_{1+} + t_1 e^{-iq_A}\Delta_{2+}}{1 - r_1 r_2 e^{-i2q_A}} + \Delta_{1-} \tag{25}$$

with equivalent expressions involving Δ_B and r_{FPB} for the other arm cavity. This again reduces the problem to a treatment of two coupled recycling cavities as depicted in Figure 13.

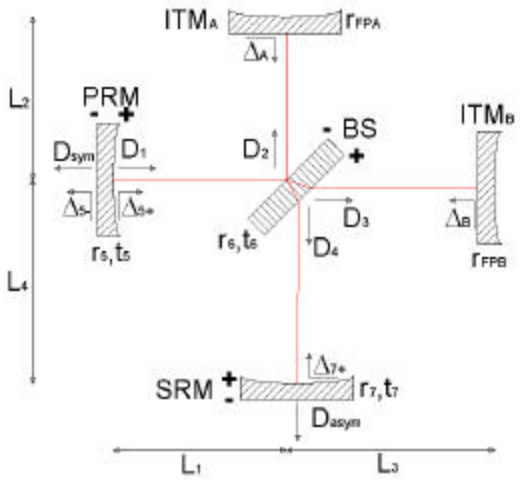

Figure 13: Variables for propagation of TEM$_{10}$ mode in the recycling cavities.

Applying the same junction conditions and slightly modified propagators

$$\exp(-iq) = \exp(-ikL + i2h), \tag{26}$$

because the TEM$_{10}$ mode accrues twice the Guoy phase shift of the fundamental Gaussian mode, we find:

$$\mathbf{M}_{jk}\mathbf{D}_k = \mathbf{T}_j \tag{27}$$

with **M** defined as above, except that all qs are now equal to $-ikL + 2ih$,

$$\mathbf{D} = [D_1, D_2, D_3, D_4]^T \tag{28}$$

and

$$\mathbf{T} = \begin{bmatrix} -r_5 r_6 e^{-i(q_1+q_2)}\Delta_A + r_5 t_6 e^{-i(q_1+q_3)}\Delta_B + \Delta_{5+} \\ t_6 e^{-iq_4}\Delta_{7+} \\ r_6 e^{-iq_4}\Delta_{7+} \\ t_6 e^{-iq_2}\Delta_A + r_6 e^{-iq_3}\Delta_B \end{bmatrix} \tag{29}$$

Solving for the components of **D** and propagating the fields to the three output ports we obtain the following expressions, analogous to (20a)-(20c):

$$D_{sym} = -t_5 r_6 e^{-i(q_1+q_2)}(r_{FPA} e^{-iq_2} D_2 + \Delta_A) + \\ + t_5 t_6 e^{-i(q_1+q_3)}(r_{FPB} e^{-iq_3} D_3 + \Delta_B) + \Delta_{5-} \tag{30a}$$

$$D_{asym} = t_7 e^{-iq_4} D_4 \tag{30b}$$

$$D_{pickoff} = t_6 r_{AR} D_3 . \tag{30c}$$

4.5. Radio Frequency Sidebands and Initial Modulation

Having derived analytical expressions for the TEM$_{00}$ and TEM$_{10}$ components of the beam at the locations where we wish to place our quadrant detector photodiodes, we can perform this calculation for each of the Fourier components we are interested in, i.e. the carrier frequency ω, and the frequencies of the sidebands $\omega \pm \Delta\omega$. The latter are imposed on the carrier by passing the beam through a Pockels cell, which we assume is placed directly in front of the PRM and phase modulates the light with a cosine term according to:

$$E_0 = E_{laser} e^{i(wt + b\cos(\Delta wt))} \approx \\ \approx E_{laser}\left[J_0(b) + 2iJ_1(b)\cos(\Delta wt)\right]e^{iwt} = \\ = E_{laser} \\ \left[J_0(b)e^{iwt} + iJ_1(b)e^{i(w+\Delta w)t} + iJ_1(b)e^{i(w-\Delta w)t}\right], \tag{31}$$

which for $\beta << 1$ reduces to

$$E_0 = E_{laser} e^{i(wt + b\cos(\Delta wt))} \approx \\ \approx E_{laser}\left[e^{iwt} + \frac{ib}{2}(e^{i(w+\Delta w)t} + e^{i(w-\Delta w)t})\right], \tag{32}$$

corresponding to a simple Taylor expansion of the second term in the complex exponential. In actual fact we require two pairs of sidebands, at $\omega \pm \Delta\omega_1$ and $\omega \pm \Delta\omega_2$. This can be achieved either by passing the beam through two Pockels cells in series or equivalently by equipping one with a

driving circuit that can resonate at both sideband frequencies. It is easy to see that (assuming equal modulation indices β for the two sidebands) this will result in:

$$E_0 = \tag{33}$$
$$= E_{laser} e^{i(wt + b\cos(\Delta w_1 t) + b\cos(\Delta w_2 t))} \approx$$
$$\approx E_{laser} e^{iwt}\left[1 + \frac{ib}{2}(e^{i\Delta w_1 t} + e^{-i\Delta w_1 t} + e^{i\Delta w_2 t} + e^{-i\Delta w_2 t})\right]$$

plus terms in β^2, which represent parasitic sidebands at difference frequencies $\Delta\omega_1 \pm \Delta\omega_2$ and $-\Delta\omega_1 \pm \Delta\omega_2$ that we can neglect because β is small. The five Fourier components at frequencies ω, $\omega \pm \Delta\omega_1$ and $\omega \pm \Delta\omega_2$ are the ones we are interested in, and we have seen above that we can trace them through the interferometer by evaluating (20a)-(20c) and (30a)-(30c) for each of them.

4.6. Demodulation at Output Ports

Having propagated both relevant modes of each frequency component to the various output ports, let us consider the alignment signals arising from the interference of the carrier at frequency ω with a pair of sidebands at frequencies $\omega \pm \Delta\omega$. At any given port we end up with an electric field of the form (setting z=0 at the output):

$$\begin{aligned}\Psi = &|E_w| \exp[i(wt - f_0 + h)] + \\ &+ |D_w| \exp[i(wt - f_1 + 2h)] + \\ &+ |E_{w+\Delta w}| \exp[i((w+\Delta w)t - f_2 + h)] + \\ &+ |D_{w+\Delta w}| \exp[i((w+\Delta w)t - f_3 + 2h)] + \\ &+ |E_{w-\Delta w}| \exp[i((w-\Delta w)t - f_4 + h)] + \\ &+ |D_{w-\Delta w}| \exp[i((w-\Delta w)t - f_5 + 2h)],\end{aligned} \tag{34}$$

where f_0 to f_5 are generic overall phases at the output port in question, and η is a Guoy phase advance we chose to artificially introduce (with the help of a Guoy phase telescope) between the output and our detector. We see that by passing the beam through a Guoy phase telescope before performing the down-conversion we introduce an effective relative phase shift between the TEM_{00} and TEM_{10} modal components. This provides, in addition to the RF demodulation phase, an extra handle on the relative strength of signals arising from different mechanical degrees of freedom.

We shall show how we can employ the phase information of the interfering Fourier/modal components to pick the optimal Guoy and RF phases for the demodulation and maximize the signal, again assuming that all interfering fields have the same beam parameter at the output and can therefore simply be treated as complex amplitudes. When we compute the intensity, which is the quantity the quad-photodiode ultimately measures, keeping only terms at the difference frequency $\Delta\omega$ and only those that make a non-zero contribution on a split photodiode after subtraction of the contributions of the two half-planes (i.e. the interference terms between TEM_{00} and TEM_{10} modes), we end up with four relevant cross terms:

$$\begin{aligned}|\Psi|^2 = &2|E_w D_{w+\Delta w}|\cos(\Delta wt - f_3 + f_0 + h) + \\ &2|E_w D_{w-\Delta w}|\cos(\Delta wt + f_5 - f_0 - h) + \\ &2|E_{w+\Delta w} D_w|\cos(\Delta wt - f_2 + f_1 - h) + \\ &2|E_{w-\Delta w} D_w|\cos(\Delta wt + f_4 - f_1 + h)\end{aligned} \tag{35}$$

plus terms at DC and frequencies greater than $\Delta\omega$. We perform the demodulation by multiplying by $\cos(\Delta\omega t - \phi)$ and averaging, which results in a signal S proportional to:

$$\begin{aligned}\Sigma \propto &|E_w D_{w+\Delta w}|\cos(-f_3 + f_0 + h + f) + \\ &+ |E_w D_{w-\Delta w}|\cos(f_5 - f_0 - h + f) + \\ &+ |E_{w+\Delta w} D_w|\cos(-f_2 + f_1 - h + f) + \\ &+ |E_{w-\Delta w} D_w|\cos(f_4 - f_1 + h + f).\end{aligned} \tag{36}$$

Recalling that the amplitudes of the TEM_{10} modes $|D|$, are proportional to the misalignment angles of the mirrors (because the source terms $|\Delta|$ are), and those of the TEM_{00} modes $|E|$, are independent of misalignments to first order, we see that we have obtained a linear and zero-crossing error signal. This is exactly what we require to implement a control system that can perform as an active null-device.

We are left with four terms and two parameters we can adjust to maximize their sum, η and ϕ. If only one pair of cross terms is significant e.g. the first two (TEM_{00} carrier against TEM_{10} sidebands), and those two terms have the same magnitude, as in the case of symmetrical sidebands, we find that the optimal choice of phases is $h_{max} = -f_0 + (f_5 + f_3)/2$ and $f_{max} = (f_3 - f_5)/2$. In this simple case:

$$\Sigma \propto \cos(f - f_{\max})\cos(h - h_{\max}), \tag{37}$$

which means that we can get rid of unwanted signals by adjusting either f_{max} or h_{max} independently. However, this ideal situation is rather rare in a system as complex as a dual-recycled interferometer, and in the majority of cases the best we can do is adjust the phases for maximal signal amplitude of the desired signal.

Note that if we had modulated with $\cos(\Delta\omega t+\xi)$ instead of $\cos(\Delta\omega t)$ in (31), we would have introduced a phase shift $\exp(i\xi)$ in the upper, but $\exp(-i\xi)$ in the lower sideband. Hence at the output we would have shifted the phases f_3 and f_5, of the upper and lower sidebands, respectively, in opposite directions, so that our choice of the demodulation RF phase f_{max} would be affected, but not the Guoy phase h_{max}, which is what we would expect.

5. Results and Discussion

5.1. Construction of Wavefront Sensing Matrices

The above analytical description of the response of the interferometer to angular misalignments and the corresponding signals being caused thereby allows us to calculate the response of potential quadrant detector photodiodes placed at the three output ports under consideration for each of the three demodulation frequencies $\Delta\omega_1$, $\Delta\omega_2$ and $\Delta\omega_2$-$\Delta\omega_1$, and for each of the six angular degrees of freedom individually, resulting in 6x9=54 potential signals. Furthermore, using the results of Section 4.6 we can calculate the optimal RF- and Guoy-phases that would maximize each of these. We have implemented this calculation in a Mathematica notebook and confirmed its validity by extensive comparisons with two other simulations of the interferometer[6].

In order to devise a sensing scheme that can be incorporated into an automatic, continuously operating alignment control system to prevent degradation of the interferometer sensitivity and that allows separate monitoring of the above six degrees of freedom, we have to construct a so-called wavefront sensing matrix relating misalignments to signal levels. This matrix has to be manifestly non-singular, and as diagonal as possible, because we need to be able to invert it in order to infer the misalignments from the measured signals in our six wavefront sensors.

For every degree of freedom we chose an output port, as well as the demodulation frequency and phases, so as to isolate the wanted signal from the other modes as far as possible. Factors to be taken into account in doing so are the absolute amplitude of the signal, the amplitude of the signal compared to the absolute power at the output port (even though the DC offset and the Fourier components at higher frequencies are removed during the lock-in like demodulation process, they nevertheless introduce noise, such that this quantity can be viewed as a signal-to-noise ratio), and the relative amplitude of the signal we want to measure with a given detector compared to those of the other, unwanted signals. To a certain extent the last point can be improved on by choosing demodulation RF phases and Guoy phase shifts wisely, such as to reduce the influence of parasite signals as far as possible.

However, while the naive application of (37) would imply one had two parameters, η and ϕ, at hand to reduce unwanted influences to zero, this is not usually the case in practice. Firstly the interferometers we are dealing with are not perfectly symmetric with respect to the upper and lower sidebands. (The detuning of the SRC, for example, introduces an asymmetry between upper and lower sidebands of the same frequency.) Secondly, for many of the signals there are not just two significant interference cross-terms, but all four are comparable and as we remarked above these two facts alter the functional dependence of the signal level on demodulation phases from the simple product of two cosines to the more complicated function of η and ϕ given by (36) which does not allow zeroing of unwanted influences by adjusting either variable independently of the other.

In practice this means that in the great majority of cases a signal from a certain degree of freedom that is contaminated with stronger signals from other misalignments will not be useful, as it will be impossible to null the latter by adjusting η and ϕ.

Having said that, we cannot possibly expect to construct a perfectly diagonal input-output matrix (wavefront sensing matrix) for our

[6] Twiddle (see [18]), a package used to calculate length sensing signals, was used to check that we had computed TEM_{00} fields in the various cavities correctly, while Modal Model (see [8]), the program that performed the relevant alignment sensing calculations for the initial LIGO configuration, was used to compare the final results directly for simple cases.

control system, which will inevitably work with a multiple-input multiple-output kernel, so combinations of two or three signals with comparable strength are still useful and indeed for most cases the best we can expect.

For the reasons outlined above, the construction of the most favorable wavefront sensing matrix is actually very intuitive, and even though optimization algorithms are easily implemented we found these almost superfluous.

Table 2 a) and b) show the resulting matrices for the current design of the 40m prototype and of Advanced LIGO, using the parameters listed in Table 1.

We assume here a modulation index of 0.1 for both sidebands, which leads to 1% of the incident beam power being distributed equally amongst the sidebands, while the remaining 99% constitute the Fourier component at the carrier frequency. Defining the effective gain necessary to extract a signal as the ratio of overall power at the detector to signal amplitude, we find that with a gain of 100dB our control scheme can reliably detect misalignments as small as 10^{-5} in units of normalized angle. This is two orders of magnitude smaller than the upper limit to rms fluctuations of $\alpha=10^{-8}$ rad or $\alpha'=10^{-3}$ given in [6] for a four kilometer initial LIGO interferometer. These considerations also set lower limits for acceptable signal levels at the outputs, which for these values of modulation index, effective gain and minimal detectable misalignment angle lie at about 10mW per Watt input power for the symmetric port, and about 3mW per Watt input power for the anti-symmetric port and pickoff.

5.2. The Pickoff as an Additional Output Port

As can be seen from Table 2, the use of the pickoff is rather limited, on the one hand because the absolute signal levels are rather low, but more importantly because this weak signal is buried in an unduly large amount of carrier light from which it has to be extracted by the demodulation process, such that the signal to noise ratio is rather unfavorable. This problem does not arise at the symmetric port, because the coupling of the carrier into the PRC is close to optimal, or at the anti-symmetric port, because the interference of the carrier is destructive there. In some cases however, the pickoff can give useful additional information.

Employing the anti-reflection coatings of the ITMs or light incident on the BS from the SRC is also possible, with the former arrangement giving information equivalent to that obtained by the arrangement depicted in Figure 11 and the latter yielding signals almost identical to those at the anti-symmetric port. Another possibility we have considered is placing detectors beyond the ETMs, which despite being designed for high reflectivity still transmit appreciable amounts of light. However, the sideband power in the arm cavities is too low to observe substantial interference with the carrier and contaminating the Fabry-Perot cavities with higher levels of RF-sideband light is not a viable option. Finally, flipping the BS such that its reflective side would face the SRM would enable us to pick off light incident from the PRM which has most of the differential information removed and might be useful to sense the PRM and the CITM mode, but this is ruled out by the fact that such a flip would increase the thermal load in the BS (by a factor of about three) due to dissipation in the substrate, which is a serious problem for high power interferometers.

5.3. Potential Problems

In constructing a wavefront sensing matrix from the available information, three basic difficulties have been identified, which do not seem to be strongly correlated, but can each pose serious problems if they appear for a certain set of parameters:

a) The SRM mode usually causes only very weak signals in any detector, which never appear in isolation, but are always accompanied by potentially dominant competitors of the PRM and the common modes. As long as we have any reasonably strong signal from the SRM and our wavefront sensing matrix remains non-singular, this is acceptable, and can be dealt with by placing the SRM at the top of the feedback hierarchy, by letting the servo zero out all the other modes first such that the only remaining signal must stem from the SRM.
b) For certain sets of interferometer parameters, all sizeable signals from the PRM and the CITM modes are degenerate, i.e. they have the same phases and appear in the same ratio. This problem is known from the initial LIGO design and led to the addition of a non-resonant sideband, which is essentially reflected straight from the PRM and never enters the interferometer, hence being sensitive to misalignments of the PRM only. In Advanced LIGO there is no need for such a

non-resonant sideband, as it is made superfluous by the presence of two resonant sidebands in combination with a sensible choice of parameters. In particular, the fact that the higher frequency pair of sidebands has a broad, symmetric resonance (i.e. the upper as well as the lower sideband are resonant), while that of the higher frequency one is narrow and asymmetric (only the upper sideband is resonant), breaks this degeneracy. Having one pair of sidebands present in the SRC to a greater extent than the other also aids this process.

c) Unless we chose our system parameters wisely, the misalignments of the two differential modes will only show up at the dark port, and furthermore all significant signals will be degenerate so that we cannot distinguish between the DETM and DITM modes. Given that these modes are the most important ones, because most prone to corrupting sensitivity or causing the interferometer to loose lock, this would be disastrous. We should not be surprised about the fact that we find degenerate signals for interference of the carrier with either of the sidebands. This is because only the TEM_{10} mode of the carrier contains information about the ETMs, as there is virtually no sideband light in the arm cavities, and for the ITMs the situation is similar. In the latter case there is actually a TEM_{10} mode of the sidebands being created as they reflect off the ITMs back into the recycling cavities. However, this is an order of magnitude smaller than the contribution from the carrier TEM_{10} originating from the ITM surfaces within the arm cavities. Hence all knowledge of the differential modes is contained in the carrier TEM_{10} light going out of the dark port and the sidebands in this case merely serve as a frequency reference to beat that first order mode against, so that it doesn't make a difference which one we use. This will always be the case at the dark port and the only remedy is to separate out the weaker contribution from the sideband TEM_{10} by putting it to the bright port, as we will see below. Note that this argument doesn't apply to the common modes, because here we observe at the symmetric port where in general the common mode signals interfere constructively and due to this constructive interference the TEM_{10} modes of the sidebands are no longer negligible, so that the degeneracy is broken.

5.4. The 40m Prototype and Advanced LIGO

For the 40m prototype, whose system parameters are by and large fixed as it is already being built, we find a reasonably diagonal wavefront sensing matrix which should be sufficient to successfully implement an alignment control scheme. The first wavefront sensor detects the strong signal of the typical combination of differential modes, irrespective of which sideband we use, while the second sensor detects the above-mentioned smaller contribution from the DITM at the bright port. There is only a weak cross-correlation between the differential modes and the other four degrees of freedom so that our matrix is almost block diagonal, but the latter group is strongly interdependent with various combinations of the common and the recycling mirror modes showing up at the bright port (and pickoff). The SRM signal is never dominant or isolated, as mentioned in a). Due to the constraints imposed on the parameters by the fact that the mode cleaner has already been installed, limiting our choice of sideband frequencies to a multiple of its free spectral range, and due to the restrictions imposed on the length of the recycling cavities by the existing vacuum envelope, this is the best we can achieve without fundamentally changing the design.

For Advanced LIGO the current design suffers from the fundamental flaw explained in c). The differential modes only show up at the anti-symmetric port and the only two appreciable signals are exactly degenerate. There is no non-intrusive way to fix this severe problem and even the addition of a third sideband would not cure it. One way out would be to look at the interference between the two sidebands to sense the motion of the ITMs, but this would require a substantial increase in sideband power to enable us to detect this weak signal, which is not desirable. The only remaining option is to change the system parameters such as to be able to detect misalignments in the ITMs at the symmetric port. The reason why this is more of a problem than for the 40m configuration is partly that for the prototype the length of the recycling cavities is appreciable compared to the arm length and hence the Rayleigh length defined by the arm cavities, so that the sidebands accrue a certain Guoy phase shift within the recycling cavities. Therefore the TEM_{10} modes propagate through the PRC and SRC in different ways from the TEM_{00} modes, which leads to a wider variety of

signals and generally less degeneracy, while this is not the case for Advanced LIGO, where the recycling cavities are very short compared to the Rayleigh length.

5.5. An Improved Set of Parameters for Advanced LIGO and a General Control Hierarchy

In searching for a viable set of parameters for Advanced LIGO, we left the transmission and reflection coefficients of the mirrors untouched, because these determine the power levels in the different cavities, which are optimized for the detection of inspirals of compact binaries and hence determined by astrophysical considerations. Instead we used only those variables that influence solely the control system, but have little effect on the operation of the interferometer as such. In particular, these are the sideband frequencies, the Schnupp asymmetry and the macroscopic lengths of the recycling cavities.

We find that the sideband frequencies are best left at their present values of 9MHz and 180MHz, because as for length sensing this large ratio of sideband wavelengths and their correspondingly different behavior in the recycling cavities seem to aid contrast between different modes and break degeneracies. It turns out that the optimal configuration is somewhat of a compromise that doesn't comply with all of the strawman design rules (1a)-(1d) outlined in Section 2. Firstly, we find that what is required to sense the DITM mode at the symmetric port is an increase of sideband power of the lower frequency sideband in the SRC up to the point where essentially both sidebands are resonant. This can be achieved by adjusting n in equation (1d) so that the length of the SRC approximately supports a resonance of the lower pair of sidebands, which entails roughly doubling the length of the SRC. There will always be an integer value for n that satisfies this condition approximately, because the resonance of the 9MHz sidebands is broad in the sense that if we adjust the cavity length microscopically to keep it locked to the carrier frequency, there will a wide range of possible values for its macroscopic length within which the sideband is approximately resonant as well. Secondly, we propose to reduce the Schnupp asymmetry from its current design value of a quarter wavelength of sideband two (~0.4m). The reason why it was thought favorable to set the Schnupp asymmetry to this particular value was that it guarantees that the power in this sideband incident from the PRC is coupled completely into the SRC. However, we find that neither this value, nor the other extreme case, namely coupling none of the higher frequency sideband power into the SRC, which would correspond to a Schnupp asymmetry of a multiple of half a wavelength, is particularly beneficial for alignment sensing. Intermediate solutions however, give good results, so we propose a value of about an eighth of a wavelength (~0.2m).

We have checked the viability of these changes with regard to length sensing by using Twiddle, a simulation written specifically for this purpose (see [18]), and found that the length control scheme is not adversely affected. This shows that even for length sensing (which is somewhat more intuitive than alignment sensing) the seemingly correct idea of improving sensitivity to the position of the SRM by having one sideband only resonant in the SRC, while almost excluding the other, and using beats between the two sidebands to sense this length degree of freedom, certainly doesn't constitute the only solution of the problem and may not be the optimal one. Notwithstanding the fact that high power levels of the sidebands in the recycling cavities are desirable and facilitate detection of deviations from the perfectly aligned state, in designing a control scheme it is not sufficient to be guided only by these considerations, but we must also look directly at the resulting length sensing signals. This is even more so for alignment sensing.

Table 2c) shows the improved wavefront sensing matrix after implementation of the above alterations. Even though the choice of demodulation phases and in some cases even the locations and demodulation frequencies of the sensors differ, the structure of the sensing matrix is rather similar to the one obtained for the configuration of the 40m prototype. For both of the investigated interferometers the control scheme boils down to the hierarchy depicted in Figure 14.

The differential modes on the one hand and the common and PRM modes on the other hand form two blocks that are only moderately interdependent. They form the foundation of the control system and only when the latter block has been successfully nulled by the servo can the SRM, which is almost independent of the differential modes but strongly interlinked with the common and PRM modes, be adjusted.

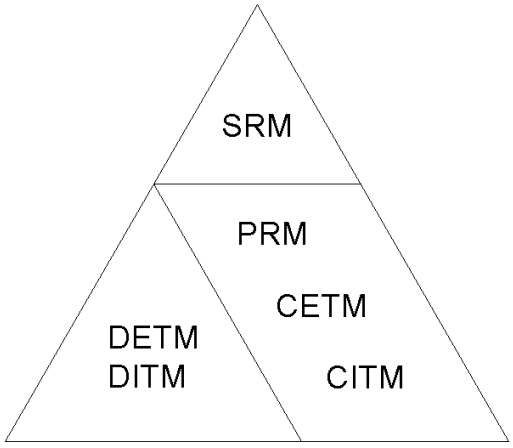

Figure 14: Feedback control pyramid.

The price we pay by moving from the initially envisioned to the improved design for Advanced LIGO is a slightly increased interdependence between the common and differential modes, but we gain two non-degenerate signals that allow us to distinguish the differential modes from each other, and hence we obtain a viable wavefront sensing scheme. We emphasize that our proposal by no means constitutes the optimal choice over the whole parameter space, but was picked from a small subset and hence there might be more scope for improvement, if one were to touch other parameters that we took as given, because they are influenced by astrophysical or technical considerations. Nevertheless this particular example demonstrates that even in a system as complex as a dual-recycled interferometer, it is feasible to implement wavefront sensing, and that two resonant sidebands are sufficient to realize a stable misalignment detection scheme.

6. Conclusions

From our results we conclude that:

a) Wavefront sensing is in principle capable of detecting misalignments with sufficient accuracy to provide, in combination with feedback loops and the actuation provided by the OSEMs, the necessary dynamical control of the angular degrees of freedom in a dual-recycled interferometer. Considering the experimental evidence of the feasibility of such a scheme presented in [19] and obtained during the implementation in initial LIGO that is currently taking place [20], we are confident that it should be possible to realize a control system based on wavefront sensing in Advanced LIGO.

b) The corresponding wavefront sensing matrix will never be diagonal, even with an optimized choice of parameters, but nevertheless manifestly non-singular and hence invertible. This necessitates a multiple-input multiple-output control system.

c) Two pairs of resonant sidebands are sufficient to discriminate between the six angular degrees of freedom of the system and there is no need for additional (resonant or non-resonant) sidebands.

d) The pickoff, which uses ghost rays to sample the light at the BS or at the ITMs, is much less useful than previously thought, due to low absolute signal levels and unfavorable ratios of signal to overall power. Only in some circumstances can the pickoff provide useful extra information.

e) The control hierarchy that crystallizes from our results entails that the common and PRM modes on the one hand, and the differential modes on the other hand can be zeroed almost independently of each other. Only when the former group has been dealt with can the servos actuate on the SRM (see Figure 14).

f) With a modulation index of 0.1 (leading to about 1% of the incoming power being pumped into the sidebands) a gain of at least 80dB of signal vs. overall power at the detector is required to be able to sense misalignments one order of magnitude smaller than the maximal allowed angle and thus ensure smooth operation of the angular alignment control system.

g) If the parameters for Advanced LIGO were to change before the final upgrade of the first generation of LIGO interferometers (and they are liable to), the redesign of length and alignment sensing/control systems would have to go hand in hand, as the optimization of the system parameters for one does not guarantee the functioning of the other.

h) Future research will have to address the question of initial alignment acquisition from a perturbed state in which the rotational motion of the mirrors is in the large angle regime, which would require a model capable of working beyond the small angle approximation and possibly even a full time domain simulation to model dynamical processes.

7. Acknowledgements

We would like to thank the personnel of the 40m laboratory at Caltech for providing an inspiring working environment and in particular Prof. A.J. Weinstein for many fruitful discussions. Also we are indebted to Prof. K. Libbrecht and the organizers of Caltech's summer undergraduate research program for having made this project possible in the first place. This work was sponsored by the US National Science Foundation.

8. Appendix – Tables

		40m Prototype	Advanced LIGO	
		Current Design	Current Design	Proposed Design
Laser Wavelength in m:	λ	$1.064\ 10^{-6}$	$1.064\ 10^{-6}$	
Transmission and reflection coefficients:	$t_1^2 = t_3^2$	0.0050000	0.0050000	
	$r_1^2 = r_3^2$	0.9949625	0.9949625	
	$t_2^2 = t_4^2$	0.0000150	0.0000150	
	$r_2^2 = r_4^2$	0.9999625	0.9999475	
	t_5^2	0.0700000	0.0750000	
	r_5^2	0.9299625	0.9249625	
	t_6^2	0.4995000	0.4998500	
	r_6^2	0.4995000	0.4998500	
	t_7^2	0.0700000	0.0700000	
	r_7^2	0.9299625	0.9299625	
	r_{AR}^2	0.0006000	0.0006000	
Radii of curvature in m:	$R_1 = R_3$	∞	54261	
	$R_2 = R_4$	57.375	54261	
Lengths in m:	L_1	0.3000	3.6267	3.6267
	L_2	2.1830	4.9090	4.8049
	L_3	1.7311	4.4927	4.5968
	L_4	0.1942	4.4435	11.9383
	L_A	38.448	4000.00	4000.00
	L_B	38.652	4000.00	4000.00
	L_{PRC}	2.2571	8.3276	8.3276
	L_{SRC}	2.1513	9.1444	16.6392
	ΔL	0.4519	0.4163	0.2081
Sideband frequencies in MHz:	$\Delta\omega_1/2\pi$	33.207	9.000	
	$\Delta\omega_2/2\pi$	166.033	180.000	
Modulation index (not optimized):	b	0.1	0.1	

Table 1: Parameters for the 40m prototype and Advanced LIGO. All lengths are optical path lengths.

a)

Port	Frequency	Guoy /°	RF/°	DETM	DITM	CETM	CITM	PRM	SRM
Antisym. Antisym.	$\Delta\omega_2$ $\Delta\omega_1$	130 149	49 85	185 104	106 59.5	0.4 0.2	0.5 0.3	-1.2 -0.7	0 0
Sym.	$\Delta\omega_1$	42	79	0	14.7	2.4	3.3	-0.9	0.3
Sym. Sym.	$\Delta\omega_2$ $\Delta\omega_1$	126 33	147 170	1.7 -2.8	3.5 -1.0	58.1 -95.7	-1.4 -36.6	19.7 -11.5	17.3 -0.5
Sym. Pickoff	$\Delta\omega_1$ $\Delta\omega_1$	108 127	175 16	-0.6 0.9	2.9 0.3	-25.2 0.1	-141 4.0	62.5 -3.5	3.4 -0.1
Sym. Sym.	$\Delta\omega_2$ $\Delta\omega_2-\Delta\omega_1$	6 103	159 140	-0.5 0	-0.2 6.0	-19.4 0.1	8.2 -44.7	-54.2 44.7	-9.9 1.4
Sym.	$\Delta\omega_2-\Delta\omega_1$	98	47	0	-1.3	0	18.9	-5.4	-10.5

b)

Port	Frequency	Guoy/°	RF/°	DETM	DITM	CETM	CITM	PRM	SRM
Antisym.	$\Delta\omega_2$	128	53	2087	1931	0	0	0	0
Antisym.	$\Delta\omega_1$	164	85	246	227	0	0	0	0
Sym.	$\Delta\omega_2$	38	70	0	4.3	-109	-58.3	-18.7	-21.3
Sym. Sym.	$\Delta\omega_1$ $\Delta\omega_2$	136 100	163 140	0 0	-2.8 -0.9	-144 64.8	-368 93.6	175 -40.9	0.4 -17.0
Sym.	$\Delta\omega_2$	98	86	0	0.9	-28.5	52.7	-73.5	-39.9
Sym.	$\Delta\omega_2-\Delta\omega_1$	157	114	0	1.2	0.3	-63.4	121	-56.8

c)

Port	Frequency	Guoy/°	RF/°	DETM	DITM	CETM	CITM	PRM	SRM
Antisym. Antisym.	$\Delta\omega_1$ $\Delta\omega_2$	106 125	172 49	1731 -1386	1602 -1282	0 0	0 0	0 0	0 0
Sym. Sym.	$\Delta\omega_1$ $\Delta\omega_2-\Delta\omega_1$	31 122	70 112	1.4 1.4	-131 -152	0.3 -1.1	-33.7 -76.3	28.1 77.6	-0.7 -3.8
Sym.	$\Delta\omega_2$	91	2	0	2.0	-184	-164	-1.1	-4.9
Sym. Pickoff	$\Delta\omega_1$ $\Delta\omega_1$	131 134	163 24	-0.9 7.9	-9.7 7.0	-177 0.5	-385 12.3	189 10.8	19.2 -0.9
Sym.	$\Delta\omega_2-\Delta\omega_1$	48	20	0.8	35.2	-2.2	249	-235	-9.2
Antisym.	$\Delta\omega_2-\Delta\omega_1$	117	4	-0.5	29.7	0.2	-53.7	4.6	47.1

Table 2: Wavefront sensing matrices with output ports, demodulation frequencies and phases for a) the 40m prototype, b) the current design for Advanced LIGO and c) the proposed design for Advanced LIGO. Significant values are given in boldface, alternatives of comparable merit in small print below. All signal levels are in mW per unit normalized angle per Watt input power.

9. Acronyms

ASC	Alignment Sensing and Control
BS	Beam Splitter
CETM	Common End Test Mass
CITM	Common Input Test Mass
DETM	Differential End Test Mass
DITM	Differential Input Test Mass
ETM	End Test Mass
ITM	Input Test Mass
LED	Light Emitting Diode
LIGO	Laser Interferometer Gravitational-Wave Observatory
Nd^{3+}:YAG	Neodymium doped Yttrium Aluminum Garnet ($Y_3Al_5O_{12}$)
OSEM	Optical Sensor Electromagnetic Actuator
PRM	Power Recycling Mirror
PRC	Power Recycling Cavity
RF	Radio Frequency
SRM	Signal Recycling Mirror
SRC	Signal Recycling Cavity
TEM	Transverse Electromagnetic Mode

10. References

[1] "Conceptual Design of the 40m Laboratory Upgrade for Prototyping an Advanced LIGO Interferometer", A. Weinstein et al., Internal LIGO technical note* LIGO-T010115-00-R (2001).

[2] "Advanced LIGO Optical Configuration and Prototyping Effort", A. Weinstein, Class. Quantum Grav., Vol. 19, 1575-1584 (2002).

[3] "Fundamentals of Interferometric Gravitational Wave Detectors", P.R. Saulson, World Scientific (1994).

[4] "Gravitational Radiation", K.S. Thorne, in "300 Years of Gravitation", S.W. Hawking and W. Israel (Editors), Cambridge University Press (1987).

[5] "The Detection of Gravitational Waves", D.G. Blair (Editor), Cambridge University Press (1991).

[6] "Alignment of an Interferometric Gravitational Wave Detector", P. Fritschel et. al., Appl. Opt. OT, Vol. 37, No. 24, 6734-6747 (1998).

[7] "Principles of Calculating the Dynamical Response of Misaligned Complex Resonant Optical Interferometers", D. Sigg and N. Mavalvala, J. Opt. Soc. Am. A, Vol. 17, No. 9, 1642-1649 (2000).

[8] "Modal Model Update" 1, 2 and 3, D. Sigg, Internal LIGO technical notes* LIGO-T960113-00-D, T960114-B-D and T960115-A-D (1996).

[9] "Quantum Noise in Second Generation, Signal-Recycled Laser Interferometric Gravitational-Wave Detectors", A. Buonanno and Y. Chen, Phys. Rev. D, Vol. 64 (2001).

[10] "Lasers", A.E. Siegman, University Science Books (1986).

[11] "Optical Electronics in Modern Communications", A. Yariv, Fifth Edition, Oxford University Press (1997).

[12] "Laser Beams and Resonators", H. Kogelnik and T. Li, Appl. Opt., Vol. 5, No. 10, 1550-1567 (1966).

[13] "Notes on the Pound-Drever-Hall Technique", E. Black, Internal LIGO technical note* LIGO-T980045-00-D (2000).

[14] "Alignment Sensing/Control Preliminary Design", P. Fritschel et al., Internal LIGO technical note* LIGO-T970060-00-D (1997).

[15] "ASC Wavefront Sensing Final Design", ISC group, Internal LIGO technical note* LIGO-T980064-00-D (1998).

[16] "Principles of Calculating Alignment Signals in Complex Resonant Optical Interferometers", Y. Hefetz et al., J. Opt. Soc. Am. B, Vol. 14, No. 7, 1597 (1997).

[17] "Alignment of Resonant Optical Cavities", D.Z. Anderson, Appl. Opt., Vol. 23, No. 17, 2944-2949 (1984).

[18] "Twiddle – A Program for Analyzing Interferometer Frequency Response", M. W. Regehr et al., Internal LIGO technical note* LIGO-T990022 (1999).

[19] "Experimental Test of an Alignment Sensing Scheme for a Gravitational-Wave Interferometer", N. Mavalvala et al., Appl. Opt. LP, Vol. 37, No. 33, 7743-7746 (1998).

[20] Fred Raab, LIGO Hanford, private communication.

* All relevant LIGO documents are available from the LIGO Document Control Center http://admdbsrv.ligo.caltech.edu/dcc/